Biosensors and Bioelectronics 166 (2020) 112439

Contents lists available at ScienceDirect

Biosensors and Bioelectronics

journal homepage: http://www.elsevier.com/locate/bios

In-situ engineered MXene-TiO_2/ $BiVO_4$ hybrid as an efficient photoelectrochemical platform for sensitive detection of soluble CD44 proteins

Razium Ali Soomro [a,*], Sana Jawaid [b], Nazar Hussain Kalawar [c], Mawada Tunesi [a], Selcan Karakuş [d], Ayben Kilislioğlu [d], Magnus Willander [e]

[a] Beijing Advanced Innovation Centre for Soft Matter Science and Engineering, Beijing University of Chemical Technology, Beijing, 100029, PR China
[b] State Key Laboratory of Chemical Resource Engineering, School of Chemistry, Beijing University of Chemical Technology, Beijing, 100029, PR China
[c] Institute of Chemistry, Shah Abdul Latif University Khairpur, 66020, Pakistan
[d] Department of Chemistry, Faculty of Engineering, Istanbul University-Cerrahpaşa, Avcılar, Istanbul, 34320, Turkey
[e] Department of Science and Technology, Campus Norrkoping, Linkoping University, SE-60174, Norrkoping, Sweden

ARTICLE INFO

Keywords:
PEC biosensor
MXene
Partially oxidized MXenes
CD44 proteins
$BiVO_4/TiO_2$ hybrid
Hyaluronic acid

ABSTRACT

Interfacial charge-carrier recombination is a bottle-neck issue restricting photoelectrochemical biosensors advancement in the wearable clinical electronics. In this study, we propose a simple approach to construct a highly efficient photoactive heterojunction capable of functioning as an active substrate in PEC biosensing of CD44 proteins. Taking the advantage of high photocatalytic activity of $BiVO_4$, and biocompatible yet conductive 2D-$Ti_3C_2T_x$ nanosheets, a workable heterojunction was constructed between in-situ formed TiO_2 from the partially oxidized $Ti_3C_2T_x$ and lysine functionalized $BiVO_4$ (TiO_2/MX-$BiVO_4$). The interfacial arrangement was ideal for promoting fast charge transfer from photo-excited $BiVO_4$ and TiO_2 to $Ti_3C_2T_x$, constructing an energy level-cascade that permits minimal charge-carrier recombination besides robust photocatalytic redox activity. The PEC biosensor relies on the ligand-protein interaction, where hyaluronic acid was directly immobilized over TiO_2/MX-$BiVO_4$ based on the interactions between carboxyl of lysine and amino moieties of hyaluronic acid. The PEC biosensor response depends on the inhibition in the measured photo-oxidation current of mediator species, i.e., ascorbic acid after the addition of CD44 proteins. The superior photo-activity, and robust heterojunction arrangement, produced a sensitive signal capable of recognizing CD44 in the wide concentration window of 2.2×10^{-4} ng mL^{-1} to 3.2 ng mL^{-1} with a low-detection limit of 1.4×10^{-2} pg mL^{-1}. The strong interaction between lysine functionalized $BiVO_4$ and hyaluronic acid enabled biosensor to exhibit robust antifouling characteristics towards similar proteins such as PSA and NSE. The quantification of CD44 protein from real-blood serum samples further confirmed the biosensor's reliability for clinical application.

1. Introduction

The photoelectrochemical (PEC) sensors have emerged as a versatile analytical tool capable of easy integration with the existing applications (Lu et al., 2020; Zhou and Tang, 2020). The separation of excitation source (light) and detection method (current) in PEC systems, provides the advantage of high signal sensitivity and low background noise. In comparison to the optical techniques, which require sophisticated interpreting programs, besides the long analysis time, the photocurrent detection method in PEC sensors is relatively simple and customizable (Chen et al., 2020b). This allows the devised sensor to exhibit superior sensitivity towards identical analytes compared to other electrochemical equivalents. As this sensitivity being, directly driven from the charge transfer process between the analyte and transducer substrate, the photoelectrode is recognized as an important component of the PEC device. Thus, the design of photoactive material and electron-capture transportation are the key factors that define the efficiency of a PEC sensor(Kong et al., 2020).

Though many attractive photoactive materials have been reported for their superior characteristics, the final PEC signal is still susceptible to the charge-carrier recombination, which is a bottle-neck issue that compromises the overall signal reliability of a PEC biosensor (Ibrahim

* Corresponding author.
E-mail address: raziumsoomro@mail.buct.edu.cn (R.A. Soomro).

https://doi.org/10.1016/j.bios.2020.112439
Received 8 April 2020; Received in revised form 7 July 2020; Accepted 8 July 2020
Available online 22 July 2020

et al., 2020). To overcome this, strategies such as elemental doping, composite-based heterojunctions, and Plasmonic sensitization have been considered (Das and Makal, 2020; Li et al., 2020b; Lv et al., 2020). Amongst these, heterojunction, particularly in-situ engineered heterojunctions have emerged as a promising system capable of controlling the charge transfer process between constituents of the hybrid composite (Huang et al., 2020b). The in-situ approach allows close defect-free interfacial contact that is capable of retarding charge-carrier recombination in addition to promoting easy interfacial charge-transportation, which improves the overall signal output (Jiang et al., 2020; Zhang et al., 2020b). Regarding heterojunction, the $TiO_2/BiVO_4$ has gained substantial attention as a superior photoactive hybrid composite due to favourable high-energy electron transfer, active catalytic redox sites, and accelerated charge-carrier separation under visible light(Polo et al., 2020; Teranishi et al., 2020). Though $TiO_2/BiVO_4$ heterojunction has gained recognition in areas such as photocatalyst, and or electrocatalyst (Fan et al., 2020; Koiki et al., 2020; Liang et al., 2020; She et al., 2020; Zhang et al., 2020c), the application of such composites in PEC biosensors is limited due to poor signal generation capability subsequent to the strong interfacial charge recombination. Besides that a PEC biosensor designed particularly for the clinical purposes require a conductive substrate such as noble metals, i.e., Au NPs or reduced graphene oxide (rGO), which can function both as an active site for redox-reaction and conductive electron sink to boost the signal response for low-concentration target analytes, i.e., biomarkers (Lu et al., 2020). The use of noble metals despite their effectiveness as active components contributes to the interfacial resistance due to its improper interfacial arrangement, thereby obstructing the interfacial electron-transportation, which eventually affects the signal reliability of the final device. Recently, the in-situ growth of TiO_2 on $Ti_3C_2T_x$ has been realized as a unique approach to produce a superior photocatalyst with minimum interfacial recombination (Han et al., 2020; Li et al., 2020a; Zhang et al., 2020a). MXenes, particularly $Ti_3C_2T_x$, with its high hydrophilicity, robust conductivity, and non-toxicity, could be envisioned as a suitable electron sink and simultaneously as a precursor substrate for in-situ growth of TiO_2 to construct $TiO_2/Ti_3C_2T_x/BiVO_4$ heterojunction(Chen et al., 2020a).

At present, the $TiO_2/Ti_3C_2T_x$ heterojunctions are limited to the partial oxidation of multi-layer MXene sheets, which given their advantages in photo-catalysis(Han et al., 2020; Huang et al., 2020a), are not suitable for PEC biosensor platform construction based on non-intimate contact between its photoactive constituents. In addition, the partial oxidation of multi-layer $Ti_3C_2T_x$ results in the formation of large TiO_2 particles at the expense of T-C bonds from $Ti_3C_2T_x$, which eventually depreciates $Ti_3C_2T_x$ larger contribution as a conducting electron-sink in the final biosensor (Sinha et al., 2018; Soleymaniha et al., 2019; Wang et al., 2017; Xiao et al., 2020). Here, the partial oxidation of few-layer thin $Ti_3C_2T_x$ sheets to form in-situ TiO_2 NPs in conjunction with nano-sized photoactive $BiVO_4$ would be a viable route to construct an efficient PEC heterojunction(Yan et al., 2019). In general, such hybrid could be envisioned for advanced PEC biosensor devices, were partially oxidized few-layer thin $Ti_3C_2T_x$ nanosheets with their non-toxic nature and high bio-compatibility could be used as photoactive immobilization substrates to produce a sensitive signal response for low-dose clinical targets(Soomro et al., 2019).

In this work, we describe the construction of photoactive heterojunction comprising of in-situ grown TiO_2 from few-layer thin $Ti_3C_2T_x$ nanosheets in conjunction with visible-light active lysine functionalized $BiVO_4$ nanoparticles. The partial oxidation of $Ti_3C_2T_x$ resulted in the formation of in-situ grown TiO_2 which in close proximity with $BiVO_4$ nanoparticles constructed an efficient photoactive heterojunction between TiO_2–$Ti_3C_2T_x$ and $BiVO_4$ ($TiO_2/MX\text{-}BiVO_4$) with conductive $Ti_3C_2T_x$ as an under-layer electron sink. The photocatalytic and electrocatalytic characteristics of $TiO_2/MX\text{-}BiVO_4$ were studied in reference to its compositional hybrids, such as partially oxidized MXene, i.e., TiO_2–$Ti_3C_2T_x$ ($MX\text{-}TiO_2$) and $BiVO_4$–$Ti_3C_2T_x$ ($MX\text{-}BiVO_4$). The $TiO_2/MX\text{-}BiVO_4$, based on its in-situ hybrid configuration, exhibited an ideal interfacial arrangement capable of supporting high photocatalytic redox-activity with minimum interfacial recombination. As a proof of concept, the photoactive hybrid was considered in the development of PEC biosensor for the detection of soluble CD44 protein, using ligand-protein interaction. The CD44 is a cellular protein found on the surfaces of a wide variety of cell types, with a vital role in cellular interactions. The abnormal expression of soluble CD44 after proteolytic cleavages has been associated with tumor progress, metastasis, and several clinicopathological parameters for cancer. Thus CD44 is considered an active biomarker for early-stage detection of a variety of cancer-related diseases. Here, hyaluronic acid (HA), a biorecognition probe with a strong affinity to CD44-proteins, was directly immobilized over $BiVO_4$ based on the interactions between $BiVO_4$ bound lysine moieties and HA. The detection of CD44 protein relayed on a stable signal response generated for the photo-oxidation of a mediator species such as ascorbic acid (AA). The inhibition in the measured photocurrent after the addition of CD44 was interpreted as the proportionate response. The constructed platform with its superior photo-activity and robust interfacial arrangement generated an enhanced signal capable of detecting CD44 in the wide concentration window of 2.2×10^{-4} ng mL^{-1} to 3.2 ng mL^{-1} with an extremely high detection sensitivity of 1.4×10^{-5} ng mL^{-1}.

The practical applicability of the newly constructed photoactive hybrid was later assessed by quantifying CD44 from real-human serum samples. The superior photocurrent response of $TiO_2/MX\text{-}BiVO_4$ demonstrated its ideal candidacy for PEC applications, whereas the $Ti_3C_2T_x$, with its high hydrophilicity and conductivity, could be envisioned as a superior and compatible substrate in PEC devises designed for biological applications.

2. Experimental section

2.1. Material and reagents

The chemicals and reagents used in this study were analytical grade. Bismuth nitrate pentahydrate ($Bi(NO_3)_3 \cdot 5H_2O$) phosphate-buffered saline (pH 7.0), and chemical like lysine (Ly; $C_6H_{14}N_2O_2$) and hyaluronic acid (HA; $(C_{14}H_{21}NO_{11})_n$) ascorbic acid (AA; $C_6H_8O_6$) was purchased from Sigma Aldrich (Germany). The Ti_3AlC_2 (MAX phase) powders (200 mesh; purity 98%) was obtained from the Beijing Forsman Scientific Co. Ltd. The CD44 proteins and other biomarkers, such as PSA and NSE, were purchased from the Novoprotein Scientific Inc. (Shanghai, China). The ITO substrates (1.5 mm thickness, 0.5×0.5 cm^2 with >90% transmittance and resistance of < 14 Ω/cm^2) were obtained from Nippon Sheet Glass, Japan. The ITO glasses were ultrasonically cleaned in de-ionized water and methanol for 30 min before their modification.

2.2. Construction of PEC biosensing substrate and measurements

The PEC active biosensor for CD44 was constructed using the ITO substrate (0.5×0.5 cm^2). Before modification, the ITO substrates were thoroughly washed with ethanol and de-ionized water. The modification was achieved by drop-casting the dispersions of $MX\text{-}TiO_2$, $MX\text{-}BiVO_4$, and $TiO_2/MX\text{-}BiVO_4$ (1 mg mL^{-1} in ethanol) over ITO surface (covered surface area of 0.4 cm^2), followed by drying under nitrogen atmosphere. A part of ITO glass was previously covered with paper-tape during modification, which was later-removed before connecting the electrodes for measurements. The surface-modified electrode, particularly $TiO_2/MX\text{-}BiVO_4$, was immersed in the HA solution (2 mg mL^{-1}) for 30 min to produce $HA\text{-}TiO_2/MX\text{-}BiVO_4$, followed by a gentle rinse with ultra-pure water. This electrode was used as a working PEC electrode for the detection of CD44 proteins. The antifouling properties of the devised electrode were evaluated by immersing the $HA\text{-}TiO_2/MX\text{-}BiVO_4$ in a fixed concentration of PSA and NSE biomarkers. The TPC measurements

were recorded for these electrodes before and after soaking of the biomarkers with CD44 (2.2×10^{-4} ng mL^{-1}). The electrocatalytic and PEC measurements were carried using an electrochemical workstation (Shanghai Chenhua Apparatus CHI830C; China) equipped with a PLS-SXE 300 xenon lamp, with a luminance intensity of 100 mW cm^{-2}. To avoid heating of the cells, the distance between the light source and cell was maintained at 12 cm. CV, EIS, and TPC measurements were recorded using a three-electrode cell with HA-TiO_2/MX-$BiVO_4$ dedicated as a working electrode, a platinum wire as the counter, and calomel (Ag/AgCl) as a reference electrode. The TPC measurement was recorded with under fixed potential of 0.3 V, and 0.1 M AA under visible light illumination for 200 s and on/off interval of 10 s with continuous argon purging of the cell to avoid air-oxidation of MXene-layer. EIS responses were measured for all the electrodes before and after the integration of biorecognition elements (HA) and soaking of biomarker (CD44) using 1.5 mM $K_3Fe(CN)_6$ electrolytic solution with a frequency range of 0.1 Hz–100 kHz.

2.3. PEC biosensing of CD44 and real samples

The constructed PEC biosensor (HA-TiO_2/MX-$BiVO_4$) was immersed in different concentrations of CD44 in a range of 2.2×10^{-4} ng mL^{-1} to 3.2 ng mL^{-1} whose response was recorded against AA, a redox mediator to produce electrocatalytic oxidation signal. The decline in the photocurrent response was calibrated to the added concentration of CD44. For the analytical precision, each concentration was determined three times, and the average photocurrent value was used to plot the calibration curve. The real-sample analysis was performed on blood samples (obtained from LMCH hospital, Hyderabad). The serum was obtained by centrifuging the samples at 3500 rpm for 60 min. The serum samples were first checked for the presence of CD44, and later known concentrations of CD44 proteins were spiked (10, 15, 20, and 25 ng mL^{-1}) followed by their quantification using HA-TiO_2/MX-$BiVO_4$ as a working electrode.

2.4. Synthesis of TiO_2-MX/$BiVO_4$ and its compositional hybrids

$BiVO_4$ was prepared using a simple wet-chemical precipitation approach. In a typical experiment, 0.6 mmol Bi $(NO_3)_3 \cdot 5H_2O$ was solubilized in 15 mL nitric acid. To this solution, 15 mL (0.025 mol/L) of Na_3VO_4 was dropped slowly under constant stirring. The solution was maintained at pH 3 under stirring for 60 min. The formed precipitates were re-dispersed in 100 mL of lysine (0.1 M) solution followed by hydrothermal treatment in a Teflon-lined stainless steel autoclave at 120 °C for 48 h. The collected $BiVO_4$ precipitates with surface-bound lysine moieties were then gently washed using ethanol and de-ionized water, followed by drying under a nitrogenous atmosphere. The positive surface charge of $BiVO_4$ allowed easy adsorption of negatively charged lysine molecules, as confirmed from the FTIR analysis. The $Ti_3C_2T_x$ nanosheets were obtained using a previous reported procedure (Sang et al., 2016; Yu et al., 2018; Zhang et al.). In a typical procedure, 1.0 g of Ti_3AlC_2 (MAX-Phase) was etched using 1.3 g of LiF in 20 mL HCl (6 M) of under 35 °C with constant staring for 24 h. The pH of the etched product was neutralized by washing it with de-ionized water. The obtained $Ti_3C_2T_x$ nanosheets were then re-dispersed in deaerated water to obtain a dispersion of 2 g/5.0 mL. To prepare MX-$BiVO_4$, the pre-prepared MXene solution was diluted with 4 mL of lysine functionalized $BiVO_4$ (0.4 g per 5 mL). The mixture was then set to agitation for 2 h followed by centrifugation to collect the MX-$BiVO_4$ hybrids.

The MX-TiO_2 was prepared using H_2O_2 induced oxidation approach. Here, 0.2 g of freshly prepared $Ti_3C_2T_x$ was dispersed in 10 mL of deaerated water, followed by slow-addition of 10 μL of 20% H_2O_2. The solution was shaken slowly, followed by separation of partially oxidized MXene using simple centrifugation. The TiO_2-MX/$BiVO_4$ was prepared by inducing partial oxidation of pre-formed MX-$BiVO_4$. The homogenous mixture of MX-$BiVO_4$ (0.4 g per 5 mL) was introduced 10 μL of 20% H_2O_2, followed by simple shaking for 10 min. The mixture was then centrifuged to obtain TiO_2-MX/$BiVO_4$, for the modification of ITO electrodes.

3. Results and discussion

The $BiVO_4$-based MXene hybrids were used to construct an efficient PEC platform capable of detecting CD44 protein with extreme sensitivity. Fig. 1 depicts the step-by-step construction of the PEC biosensing platform. Initially, the dispersion of partially oxidized MXene with lysine-functionalized $BiVO_4$ was drop-casted on ITO electrodes. This electrode was later immersed in a solution of HA, which, given the interaction between lysine and HA, was immobilized as a biorecognition element for CD44. The electrode was then immersed in different concentrations of CD44 protein before PEC measurements.

The chemical and structural superiority of TiO_2/MX-$BiVO_4$ was proven by competitive measurements against its compositional counterparts, such as partially oxidized MXene (MX-TiO_2) and $BiVO_4$ NPs adsorbed over $Ti_3C_2T_x$ (MX-$BiVO_4$). Fig. 2 shows the corresponding TEM images of the hybrids in reference to the pristine $Ti_3C_2T_x$ nanosheets. Unlike pristine $Ti_3C_2T_x$, with smooth, thin sheet-like morphological features (Fig. 2(a)), the MX-TiO_2, consists of TiO_2 nanoparticles dispersed throughout the entire volume of the sheet. The use of H_2O_2 resulted in homogenous partial-surface oxidation of $Ti_3C_2T_x$ sheet, with in-situ formation of TiO_2 nanoparticles (Fig. 2(b)). In comparison, the MX-$BiVO_4$ hybrid shows no evidence of surface oxidation after the surface adsorption of $BiVO_4$ nanoparticles (Fig. 2(c)). $BiVO_4$ nanoparticles were well-dispersed over thin $Ti_3C_2T_x$ nanosheet, without causing any fractures or oxidized TiO_2 domains. The small average diameter of $BiVO_4$ (6.5 ± 1.5 nm) with dangling NH_3 moieties (from lysine) resulted in a strong surface-bound interaction with hydrophilic $Ti_3C_2T_x$ (discussed below). Fig. 2(d–f) shows the TEM images for TiO_2/MX-$BiVO_4$ hybrid, where partially oxidized $Ti_3C_2T_x$ sheets with amorphous TiO_2 nanoparticles in intimate contact with $BiVO_4$ NPs can be witnessed. The high magnification TEM image provided in Fig. 2 (f) shows a close-up view of the constructed compact interfacial heterojunction between $BiVO_4$ NPs and in-situ formed TiO_2 from the partially oxidized $Ti_3C_2T_x$ nanosheets. Since the partial oxidation of $Ti_3C_2T_x$ was initiated after the adsorption of $BiVO_4$ NPs, the in-situ formed amorphous TiO_2 has compacted with the $BiVO_4$ NPs where the thin $Ti_3C_2T_x$ nanosheet acts as an underlying conductive blanket to facilitate the charge-carrier movement during the photocatalytic redox reaction.

The XRD analysis further confirmed the partial oxidation and co-existence of $BiVO_4$ with TiO_2/$Ti_3C_2T_x$. The MX-TiO_2 consisted the characteristics peaks of TiO_2 at 25° and 37.8°, 48.2°, and 54.1° indexed to the (101), (004), (200), and (211) planes of TiO_2-anatase respectively (ICDD No. 71–1166), besides the typical (002) peak at 7.3° and (004), (0010), (0012) peaks of $Ti_3C_2T_x$ (Fig. 3 (a)). In comparison, the TiO_2/MX-$BiVO_4$ comprised of characteristics peaks related to $Ti_3C_2T_x$ and TiO_2 together with an additional peaks identified at 19.1°, 28.8°, 34.6°, 39.9°, 46.7°, 47.2°, 53.2°, and 55.9°, which were indexed for (011), (112), (004), (200), (211), (204), (024), (116), and (215) planes of monoclinic $BiVO_4$ (JCPDS No.14–0688) respectively(Shi et al., 2018). Although, no evidence of carbon component was observed, probably because of its very low content. The presence of characteristic peaks of partially oxidized $Ti_3C_2T_x$ in combination with $BiVO_4$ justifies their co-existence as in a hybrid configuration(Liu et al., 2017).

The Raman analysis of TiO_2/MX-$BiVO_4$ in reference to its compositional counterparts is shown in Fig. 3(b–c). Here, the MX-TiO_2 portrayed a typical profile of partially oxidized $Ti_3C_2T_x$ with bands at 197, 292, 392, 632, and 710 cm^{-1} and 144, 398.7, 518 and 642 cm^{-1} which correspond to vibration frequencies of $Ti_3C_2T_x$ and in-situ formed TiO_2 respectively (Fig. 3(b)). Unlike MX-TiO_2, the MX-$BiVO_4$ exhibited no evidence of surface oxidation, besides the presence of prominent $BiVO_4$ bands at 125, 206, 326, 366, 710, and 827 cm^{-1} (Fig. 3(c)). The Raman spectra for TiO_2/MX-$BiVO_4$ confirmed the presence of all-bands typical

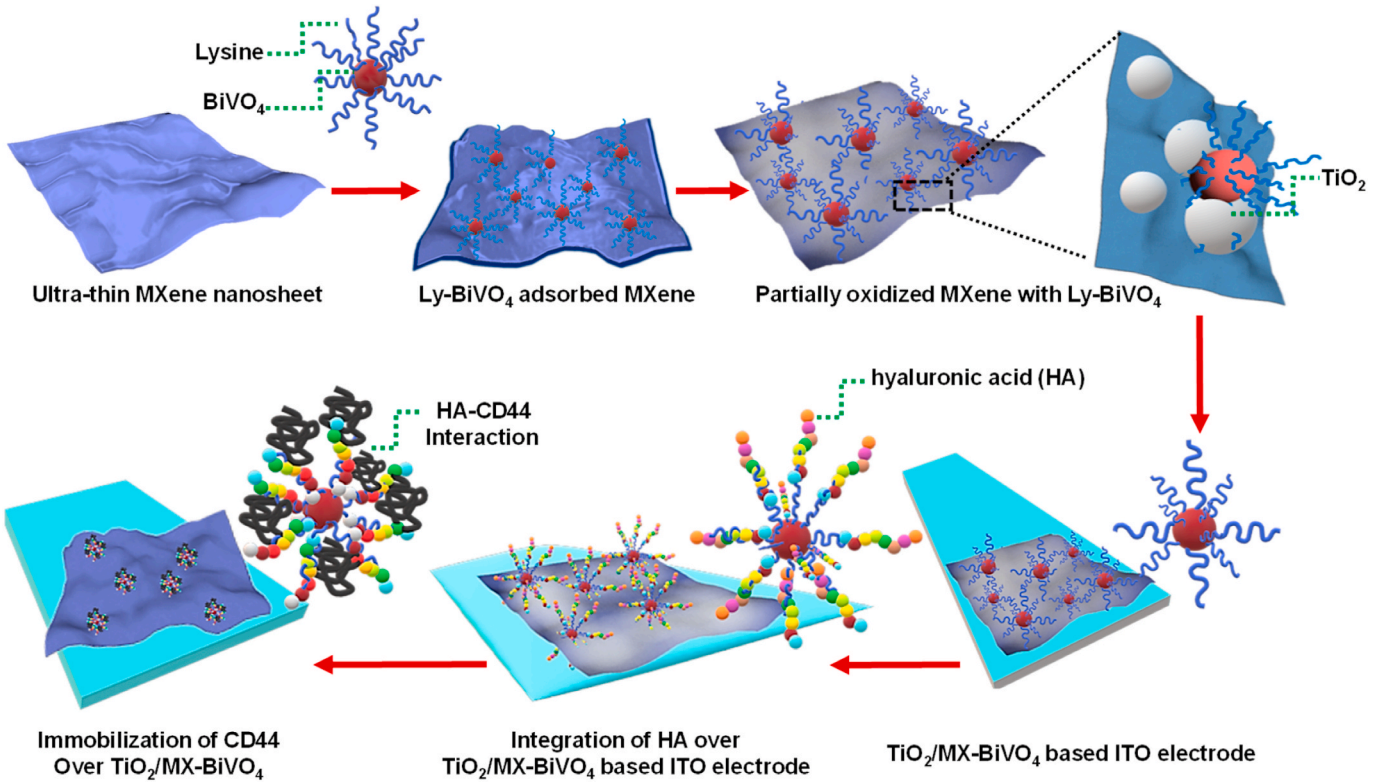

Fig. 1. A schematic diagram depicting step-by-step construction of the TiO_2/MX-$BiVO_4$ based PEC biosensor for CD44 protein. Lysine-functionalized $BiVO_4$ were adsorbed on few-layer thin MXene nanosheets, whereby the partial surface oxidation induced by H_2O_2, lead to the formation of TiO_2/$Ti_3C_2T_x$/$BiVO_4$ heterojunction. To construct the biosensing platform, ITO electrodes were then immersed in a solution of hyaluronic acid (HA), a biorecognition element, and then in different concentrations of CD44 solution for PEC measurement.

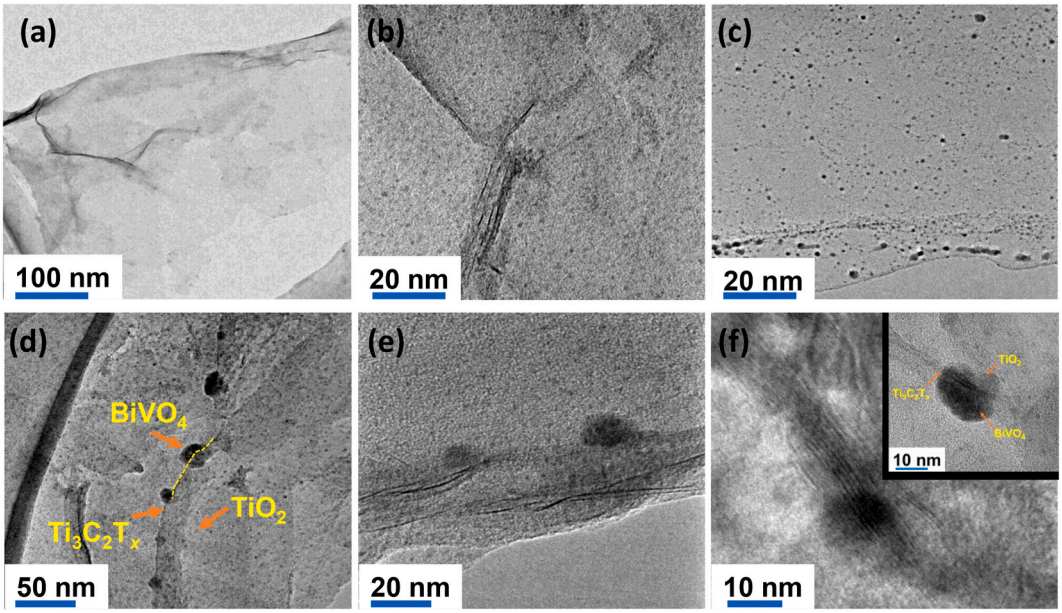

Fig. 2. TEM images (a) pristine $Ti_3C_2T_x$ nanosheets; (b) partially oxidized $Ti_3C_2T_x$ (MX-TiO_2) with in-situ formed TiO_2 nanoparticles; (c) hybrid of $Ti_3C_2T_x$ nanosheets with lysine functionalized $BiVO_4$ (MX-$BiVO_4$); (d–e) different magnification of TiO_2/MX-$BiVO_4$; (f) high-resolution capture showing the corresponding interface formation with inset figure depicting the close-up view of the intimate contact between the constituent components like $BiVO_4$, in-situ formed TiO_2 and $Ti_3C_2T_x$.

of $Ti_3C_2T_x$, $BiVO_4$, and TiO_2 (Fan et al., 2020; Yan et al., 2019). However, the strong 144 cm^{-1} band attributed to TiO_2 was found slightly shifted to a higher frequency (149 cm^{-1}), which specifies the interaction between in-situ formed TiO_2 and surface-bound $BiVO_4$ (Fig. 3(c)). Such interaction are highly desirable to obtain an intimate-interfacial contact which would later support in an efficient charge-carrier separation process during photocatalytic redox reaction (Su et al., 2019; Zhang et al., 2019). These surface-bound interactions were also established

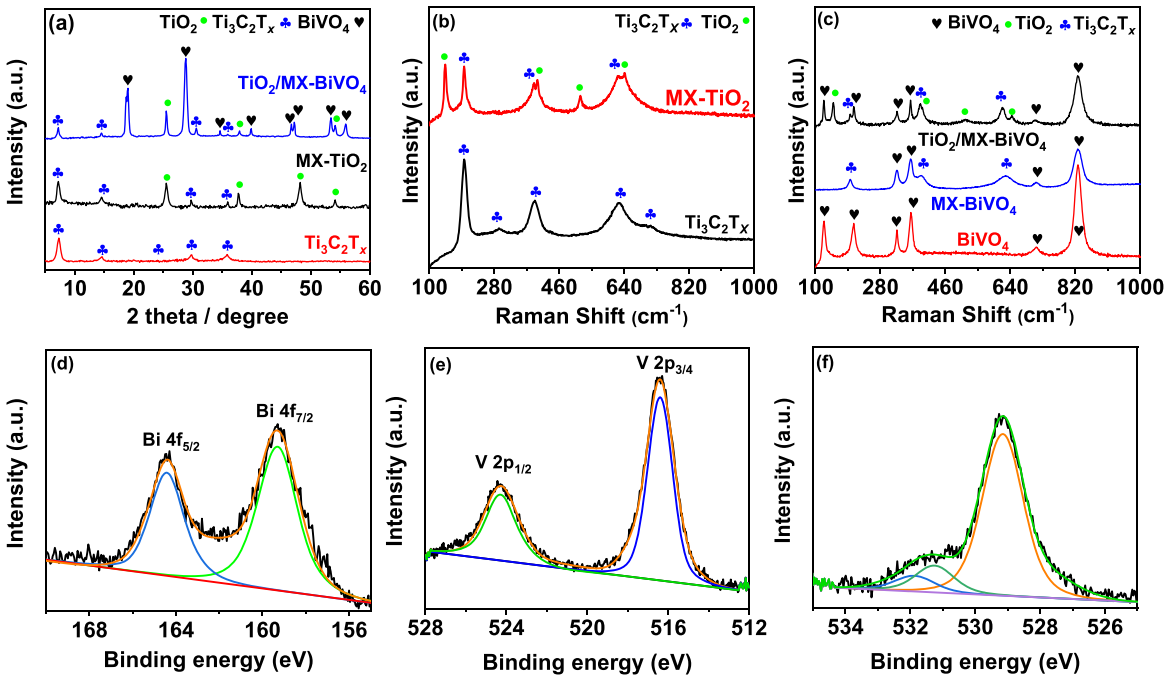

Fig. 3. (a) XRD patterns and (b–c) Raman spectra for TiO_2/MX-$BiVO_4$ in reference to pristine $Ti_3C_2T_x$, MX-TiO_2 and MX-$BiVO_4$ (d–e) the XPS high-resolution profiles for Bi, V and O elements of pristine $BiVO_4$ NPs.

using XPS analysis. Fig. 3(d–f) shows the high-resolution binding energies XPS spectra for Bi, V, and O elements of pristine $BiVO_4$. Here the Bi 4f $_{7/2}$ and Bi 4f $_{5/2}$ were observed at 159.3 and 164.4 eV, confirming the existence of Bi as Bi $^{3+}$, whereas the V2p $_{1/2}$ and V2p $_{3/2}$ doublets were identified at 524 and 516.3 eV respectively (Fig. 3(e–f)). The O1s spectra displayed a strong peak at 529.9 eV along with weak companions at 531.1eV, and 531.8 eV attributed to the $BiVO_4$ lattice oxygen and hydroxyl moieties associated with metal cation and or chemisorbed oxygen species of water molecules (Fig. 3(f)). The generated XPS profile was in complete agreement with studies related to the surface analysis of $BiVO_4$(Guo et al., 2016).

The Ti 2p high-resolution XPS fitting profile for MX-$BiVO_4$ revelled major bands at 455.0 (461.7), 455.9 (462.0), 457.0 (462.5), and 460 eV which were associated with Ti, Ti $^{2+}$, Ti $^{3+}$, and C–Ti bond of $Ti_3C_2T_x$ respectively. In addition, a strong band near 466 eV evolved, attributed to the Bi 5d orbit of surface-bound $BiVO_4$(Su et al., 2019). The Ti2p profile shows no evidence of surface oxidation of $Ti_3C_2T_x$, as the typical TiO_2 bands (458 and 462 eV) were found absent (Fig. 4(a)). The C1s

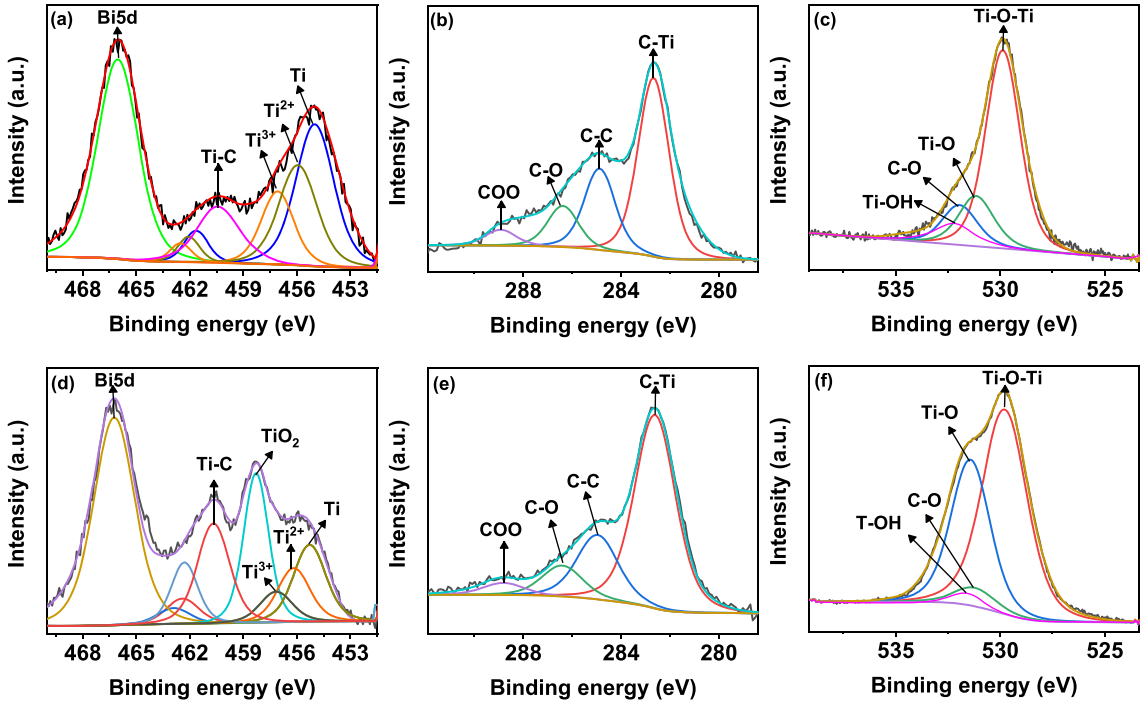

Fig. 4. The high-resolution XPS profiling of Ti2p, C1s, O1s for (a–c) MX-$BiVO_4$ with no evidence of surface oxidation of $Ti_3C_2T_x$; and (d–f) TiO_2/MX-$BiVO_4$ with characteristics bands for the partial oxidation of $Ti_3C_2T_x$ (in- situ formation of TiO_2).

spectra consisted of four energy bands (281.5, 284.8, 286.4, and 288.7 eV), which were assigned to C-T, C–C, C–O, and COO bonds of $Ti_3C_2T_x$ (Fig. 4(b)). In addition, the O1s spectra consist of a strong band at 529.7 along with weak bands near 531.2, 531.6, and 532.0, attributed to Ti–O–Ti, T-O, Ti–OH, and terminal C–O bonds of $Ti_3C_2T_x$ (Zalfani et al., 2015)(Fig. 4(c)). Contrary to MX-$BiVO_4$, a strong TiO_2 bond energy peak was observed in the high-resolution Ti 2p spectrum of TiO_2/MX-$BiVO_4$ besides the typical Bi and MXene energy bands (Fig. 4(d)). A notable slight shift in the binding energy of TiO_2 and Bi from 458.0 and 466.0 to 458.3 and 466.7 eV was observed in the case of TiO_2/MX-$BiVO_4$, which further confirmed the interaction between the in-situ formed TiO_2 and surface bound $BiVO_4$ NPs. In addition, a significant decline in the intensity of C-T bond in the corresponding C1s spectra together with an increase in T-O bond energy (O1s spectra) of TiO_2/MX-$BiVO_4$ indicate that the in-situ TiO_2 dominions were formed at the expense of surface oxidation of C-T bonds of $Ti_3C_2T_x$ nanosheets (Fig. 4(e–f)). The XPS profiling was in complete agreement with the Raman analysis, justifying the surface bound interaction of $BiVO_4$ with the in-situ formed TiO_2 (partial oxidized $Ti_3C_2T_x$) and successful construction of the $BiVO_4$/-TiO_2/$Ti_3C_2T_x$ heterojunction (TiO_2/MX-$BiVO_4$). The optical characteristics of the constructed photoactive heterojunction were obtained using UV–Vis and PL spectroscopy. Fig. S2 (a) shows the adsorption edge of TiO_2/MX-$BiVO_4$ in comparison to other compositional constituents. The pristine $BiVO_4$ and TiO_2 had an adsorption edge near 522 and 385 nm, which correspond to the bandgap energy (E_g) of 2.23 and 2.97 eV (Fig. S2 (b)). Unlike pristine TiO_2, the MX-TiO_2 shows an increase in absorption edge with a bandgap shift from 2.98 to 2.85 eV, whereas TiO_2/MX-$BiVO_4$, exhibited an adsorption edge near 530 nm with a lower bandgap value of 2.10 eV compared to the MX-$BiVO_4$ (2.21 eV) (Sun et al., 2015). The narrowing of bandgap with increased adsorption edge confirms the enhanced visible-light absorption capability of the hybrid subsequent to the synergic coupling of partially oxidized MXene and $BiVO_4$. The charge-transfer behaviour in the prepared hybrid composite (TiO_2/MX-$BiVO_4$) was deduced using Mott-Schottky (M-S) plots and PL-spectroscopy. The M-S plots are indicative of flat band potential, which is related to the conduction band of n-type semiconductors. Fig. S2 (c) shows the M-S plots for MX-TiO_2 in reference to pristine TiO_2. As the C.B of TiO_2 (-0.68) is more negative compared to the MX-TiO_2 (-0.28), easy electron transfer could be anticipated from TiO_2 to $Ti_3C_2T_x$ (electron sink). In the case of TiO_2/MX-$BiVO_4$, (Fig. S2 (d)), the C.B was found, relatively more negative (-0.02) compared to the pristine $BiVO_4$ (0.05) and MX-$BiVO_4$ (0.02), which confirmed the electron transfer feasibility from the composite ($BiVO_4$–TiO_2) to $Ti_3C_2T_x$ respectively.

The corresponding band-energy structures for TiO_2; MX-TiO_2, and $BiVO_4$; MX-$BiVO_4$ are shown as an inset of Figs. S2(c–d). The estimated valance band potentials (V.B) of MX-TiO_2 (3.13 eV) and MX-$BiVO_4$ (2.19 eV) were found relatively less positive than their pristine counterparts (TiO_2 (3.65 eV), $BiVO_4$ (2.28 eV)), which further confirms the favourable h^+ transfer from photoactive TiO_2 to $BiVO_4$. The designed configuration is effective in accelerating the charge-carrier mobility, whereby the formed Schottky-barrier contributes to the reducing of charge-carrier recombination at the formed interfaces, allowing the photo-generated (h^+) to efficiently participate in the photocatalytic oxidation reaction(Sun et al., 2019a). These results were further

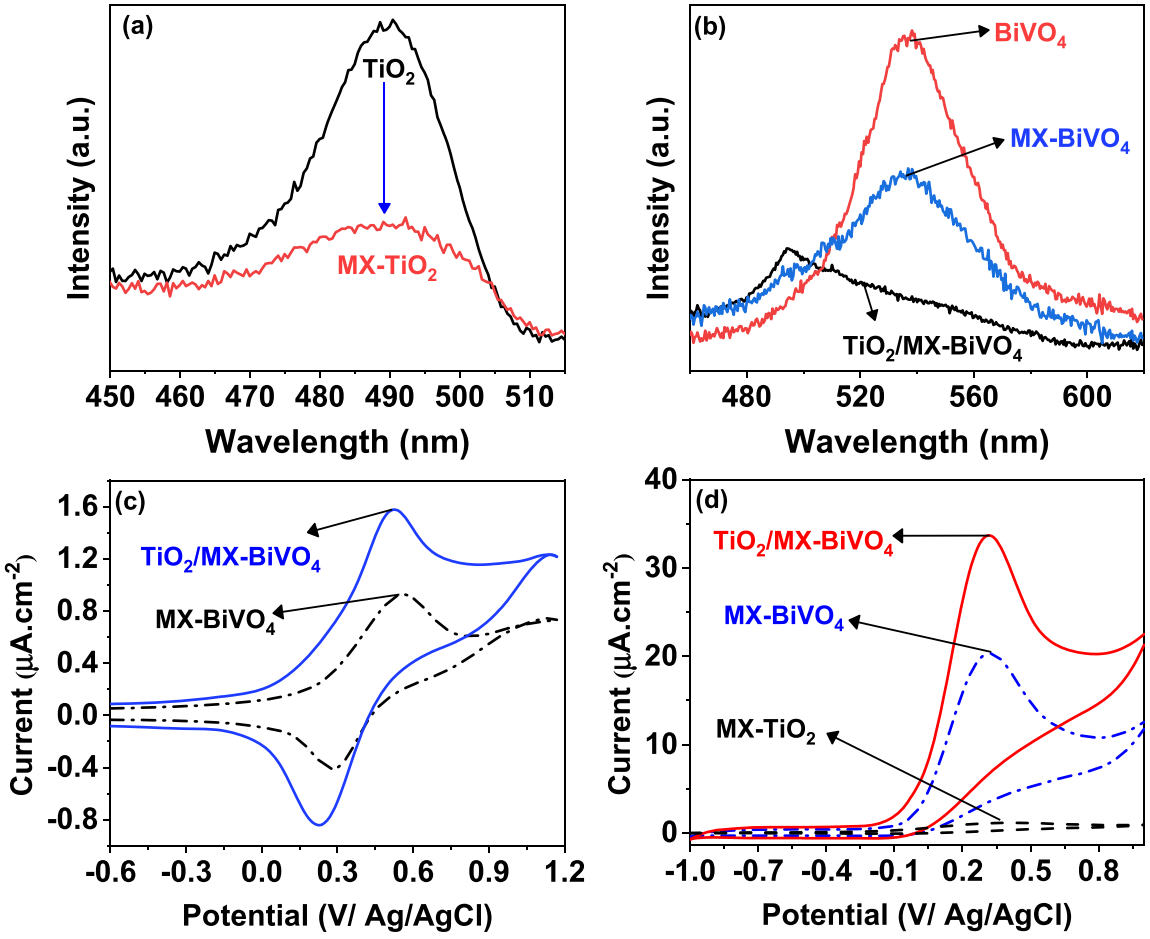

Fig. 5. (a–b) the PL-spectra for MX-H_2O_2, MX-$BiVO_4$ and TiO_2/MX-$BiVO_4$ in reference to pristine TiO_2 and $BiVO_4$; (c) the CV curve recorded for TiO_2/MX-$BiVO_4$ (*dash-dot-dash*) and MX-$BiVO_4$ (*line*) in 0.1 M PBS (pH = 7.0) using a scan rate of 0.05 V^{-1}; (d) CV curve for the electrocatalytic oxidation of ascorbic acid (AA) (0.1 mM) using TiO_2/MX-$BiVO_4$ (line), MX-$BiVO_4$ (*dash-dot-dash*) and MX-TiO_2 (dashed).

validated using PL-spectroscopy. Fig. 5(a) shows the PL spectra of MX-TiO_2 in reference to pristine TiO_2. The declined PL intensity in the case of MX-TiO_2 near the excitation band of pristine TiO_2 (490 nm) is the evidence that the $Ti_3C_2T_x$ can significantly contribute to the suppression of electron-hole recombination(Sun et al., 2019b). A decline in the PL band intensity near 525 nm, typical of the $BiVO_4$ was also observed in the case of TiO_2/MX-$BiVO_4$ (Fig. 5(b)). This indicates that the coupling of partially oxidized $Ti_3C_2T_x$ with $BiVO_4$ in a hybrid a configuration could efficiently suppress the charge-carrier recombination based on the intimate interfacial contact between the compositional constituents, i.e., $Ti_3C_2T_x$-TiO_2 and $BiVO_4$.

The electrochemical characteristics were later deduced to highlight the redox capability of the devised hybrid before the integration of the bio-recognition element (HA) for CD44 detection. Fig. 5(c) shows the CV response of MX-$BiVO_4$ and TiO_2/MX-$BiVO_4$ measured in 0.1 M PBS (pH 7.0) under the fixed scan rate of 0.05 V^{-1}. In comparison to pristine $BiVO_4$, which shows a weak Bi (III/II) redox couple at 0.61/0.30 V (Fig. S1 (a)) (Derbali et al., 2020; Wang et al., 2019), a slight low-potential shift to 0.56/0.28 V with an increase in current intensity to 0.92 μA cm^{-2} was observed in the case of MX-$BiVO_4$. This improvement could be attributed to the integration of highly conductive $Ti_3C_2T_x$ with $BiVO_4$. Further enhancement was achieved in the case of TiO_2/MX-$BiVO_4$, where the redox couple shifted to a lower voltage value of 0.52/0.23 V with an increase in current intensity to 1.5 μA cm^{-2}, signifying the superior electrocatalytic performance of the hybrid based on the synergic coupling of $BiVO_4$ with partially oxidized $Ti_3C_2T_x$. Fig. S1 (b) shows the CV curve of MX-TiO_2 with a strong peak near 0.8 V, which could be associated with complete oxidation of $Ti_3C_2T_x$ in TiO_2. Thus, to avoid anodic oxidation of $Ti_3C_2T_x$ within the hybrid (TiO_2/MX-$BiVO_4$), a low-potential oxidizing molecule such as ascorbic acid (AA) was used as a probing agent for the in-direct detection of CD44 protein. Fig. 5(d) shows the CV response for the electrocatalytic oxidation of AA, using TiO_2/MX-$BiVO_4$, with an enhanced current response of 33.6 μA cm^{-2} in comparison to MX-$BiVO_4$ (20.2 μA cm^{-2}) and MX-TiO_2 (2.1 μA cm^{-2}) respectively. In case of pristine $Ti_3C_2T_x$ no prominent redox peak (Fig. S1 (c)) was noted, indicating its poor capability to oxidize AA in PBS electrolyte.

The robust response of TiO_2/MX-$BiVO_4$ confirms its capability to perform as an efficient electrocatalytic platform for PEC biosensors. The photocatalytic performance was further evaluated using transient photocurrent (TPC) measurement recorded with a fixed potential of 0.3 V and 0.1 mM AA under visible light illumination for 200 s and on/off interval of 10 s (Fig. S4 (a)). The current response of TiO_2/MX-$BiVO_4$ was obtained after optimization of typical parameters such as the concentration of AA, electrolytic pH, and loading of electrocatalyst (TiO_2/MX-$BiVO_4$) (Figure S3 (a-c)). The high current generation and steady response proved the enhanced charge-separation capability of TiO_2/MX-$BiVO_4$. Here, the TiO_2/MX-$BiVO_4$ generated a photocurrent density of 183.0 μA cm^{-2}, followed by appsec1 MX-$BiVO_4$(91 μA cm^{-2}), MX-TiO_2 (23 μA cm^{-2}) and $BiVO_4$ (11.6 μA cm^{-2}). The high transient current response is directly related to the firm interfacial contract between the components of the hybrid, which, along with accelerated charge-carrier production, facilitate their rapid surface mobility with minimum interfacial recombination.

The hyaluronic acid (HA) was later immobilized over TiO_2/MX-$BiVO_4$ to configure it with the bio-recognition ability to detect CD44 proteins. As the prepared $BiVO_4$ NPs were primarily functionalized with lysine moieties, strong immobilization of HA over $BiVO_4$ could be expected based on carbonyl-amine bond (Carneiro et al., 2016; de Oliveira et al., 2017), as confirmed from the FTIR analysis (Figure S4 (b-c)). The FTIR spectrum of pristine $BiVO_4$ and its lysine functionalized counterpart (Ly-$BiVO_4$) is shown as Fig. S4 (b). The typical bands for $BiVO_4$ included V═O vibration stretching at 847 cm^{-1}, symmetric stretching mode of V–O–V at 523 cm^{-1}, and finally, O–H stretching and bending of lattice water molecules at 3402 and 1627 cm^{-1} respectively(Zulkifili et al., 2018).

The typical bands of lysine were identified at 3420 cm^{-1} for N–H, C–H at 2960 cm^{-1}, 1617, and 1420 cm^{-1} for symmetric and asymmetric vibration of COO^-. The bands at1509 and 1566 cm^{-1} corresponded to asymmetric bending of NH3+ and vibration of COO^- respectively(Antal et al., 2018). In the case of Ly-$BiVO_4$, a shift in the vibrational frequencies of COO^- from 1617 cm^{-1} to 1627 $cm^{-1}$and 1420 cm^{-1} to 1440 cm^{-1} confirmed the surface interaction of lysine with $BiVO_4$ via carboxyl moieties. The typical V═O and V–O–V vibration of $BiVO_4$ were identified at 845 and 520 cm^{-1}, respectively. In addition, the band at 509 cm^{-1} and 1566 cm^{-1} further indicted the availability of NH3+ moieties for the attachment of HA. This was later confirmed from the FTIR spectrum of Ly-$BiVO_4$ after the immobilization of HA, where typical bands of carboxylic stretching disappeared, and a new band near 2625 cm^{-1} appeared (Fig. S3(b)). This band could be attributed to quaternary ammonium salt (NR^{4+} group), which is typical of HA-lysine interaction(Carneiro et al., 2016). The provided FTIR analysis supports the interaction of HA with lysine functionalized $BiVO_4$. Thus, it is safe to assume that the immobilization of HA over TiO_2/MX-$BiVO_4$ hybrid could be achieved via the interaction between carboxyl groups of HA and amine from Ly-$BiVO_4$ as graphically represented in Fig. 1.

EIS confirmed the successful immobilization of HA over TiO_2/MX-$BiVO_4$. Fig. S3 (d) shows the Nyquist plot recorded for HA immobilized TiO_2/MX-$BiVO_4$ (HA-TiO_2/MX-$BiVO_4$) in reference to MX-$BiVO_4$. A gradual increase in charge transfer resistance was achieved on going from MX-$BiVO_4$ to HA-TiO_2/MX-$BiVO_4$, confirming the successful integration of HA over the PEC active hybrid (TiO_2/MX-$BiVO_4$). To achieve maximum detection sensitivity, the immobilization time, and the concentration of HA were optimized. The maximum inhibition in the transient photocurrent oxidation signal of AA could be achieved when the immobilization concentration and time of HA were maintained at 0.5 mg mL^{-1} 30 min, respectively (Fig. S3 (d)). The quantification of CD44 protein was carried under the optimum conditions, where the constructed PEC electrode (HA-TiO_2/MX-$BiVO_4$) was first immersed in different concentrations of CD44 in the range of 2.2 × 10^{-4} ng mL^{-1} to 3.2 ng.mL^{-1}prior to photocurrent measurements within 0.1 mM AA in 0.1 M PBS (pH 7.0). Fig. 6 (a) shows the measured photocurrent inhibition obtained against the different concentrations of CD44 proteins. Fig. 6(b) shows the logarithmic relationship between the measured photocurrent and the increasing concentration of CD44. The corresponding calibration is shown as Fig. 6(c), where the logarithmic relationship between inhibited photocurrent and concentration could be defined using the following equation I = -28.5 log(x) +46.9 (R^2 = 0.9855). The high signal sensitivity attributed to the ideal heterojunction configuration of TiO_2/MX-$BiVO_4$ allowed a low detection limit of 1.4 × 10^{-5} ng mL^{-1} (S/N = 3) for CD44 proteins. The wide detection window and low detection limit achieved using TiO_2/MX-$BiVO_4$ are relatively superior compared to the other competitive biosensors for CD44 (Table S1). Fig. 6(d) shows an illustration of the engineered heterojunction with charge transfer representation for the electrocatalytic oxidation of the mediator species (AA). Here the photo-generated charge carriers (h^+) were responsible for the oxidation of AA, whereby the produced electrons cascade from the conduction bands of $BiVO_4$ and TiO_2 to the MXene layer which boosts up the charge transfer process resulting in a robust current response. The response then declines with the addition of CD44 protein, which, based on its strong affinity towards HA, leads to the blockage of charge-transfer and signal suppression, as illustrated in the lower region of the schematic diagram.

As the devised sensor system relies on the strong interaction between HA with CD44, strong antifouling characteristics could be anticipated for the HA-TiO_2/MX-$BiVO_4$. Fig. S5 (a) shows the bar-graph plotted for the transient photocurrent response of TiO_2/MX-$BiVO_4$ with 0.8 mM AA, and minimal concentration of CD44 (2.2 × 10^{-4} ng mL^{-1}) along with common biofouling agents such as PSA, and NSA biomarkers with a concentration similar to CD44. The minimal signal fluctuation in the photocurrent response despite the presence of structurally similar antigens proves the strong antifouling characteristics of the devised sensor.

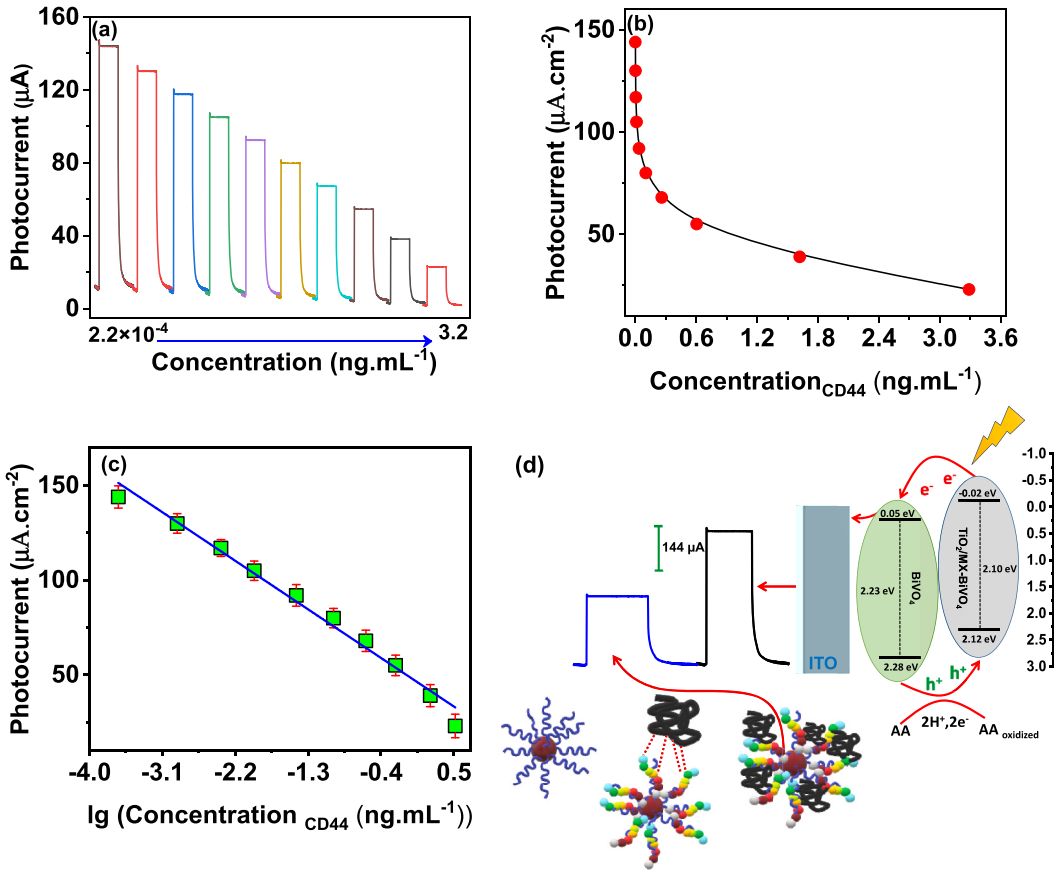

Fig. 6. (a) The transient photocurrent inhibition response of HA-TiO_2/MX-$BiVO_4$ post immersion in different CD44 concentration; (b) the corresponding photocurrent decline with the added concentrations of CD44; (c) The calibration plot that defines the logarithmic relationship between inhibited photocurrent and concentration of CD44 in range of 2.2×10^{-4} ng mL^{-1} to 3.2 ng mL^{-1}; (d) schematic illustration of the constructed photoactive heterojunction showing the cascade of electron-transfer subsequent to oxidation of AA and its enhanced photocurrent with estimated energy level for TiO_2/MX-$BiVO_4$ and $BiVO_4$ in hybrid configuration. The lower section shows the drawing depicting the inhibitory molecular interaction between CD44 proteins and HA-immobilized $BiVO_4$ NPs and the corresponding photocurrent suppression.

The resilient selectivity, in this case, can be explained based on relatively strong interactive forces between HA and CD44 ligand, which in combination with highly photoactive hybrid (TiO_2/MX-$BiVO_4$) constructs a highly robust yet selective CD44 biosensor. The signal reproducibility and storage stability of the constructed biosensor was also evaluated. Figure (S5(b)) shows the normalized current response measured for 5 similarly constructed biosensors against a standard CD44 sample (2.2×10^{-4} ng mL^{-1}). The signal fluctuation for each electrode was negligible, indicating the robust signal reproducibility of the electrode. In the case of storage stability, the signal response was measured after storing the HA-free TiO_2/MX-$BiVO_4$ for three consecutive weeks. The post-storage response was measured after immobilization of HA against CD44 protein with a standard concentration of 2.2×10^{-4} ng mL^{-1}.The normalized response confirmed a signal decline of 1.8, 3.5 and 5.7% during the 3 weeks of storage. The slight decrease in the photocurrent response could be associated with the slow-transformation (oxidation) of $Ti_3C_2T_x$, resulting in loss of conductive bed, and thus the photocurrent. The overall current response was maintained at 90%, throughout the storage period, reflecting the long-term shelf-life of the devised PEC biosensor.

The HA-TiO_2/MX-$BiVO_4$ was then used for the determination of CD44 protein from human serum samples. Table S2 shows the analytical recovery data of different spiked samples. The low relative standard deviation and high recovery justify the practical capability of the devised PEC biosensor for clinical purposes.

4. Conclusion

A workable heterojunction was constructed between in-situ formed TiO_2 from $Ti_3C_2T_x$ and photoactive $BiVO_4$ NPs, previously functionalized with lysine (TiO_2/MX-$BiVO_4$). The photo-active hybrid composite was later utilized in the development of PEC biosensor for the detection of CD44 protein, a cancer biomarker, using the ligand-protein interaction strategy. The high photo-catalytic activity coupled with robust conductivity of under layered MXene sheets ($Ti_3C_2T_x$), resulted in a robust electrochemical oxidation signal for redox mediator, i.e., ascorbic acid (AA). The inhibition in the measured response against addition of CD44 was considered the primarily signal. The devised PEC biosensor exhibited wide working range of 2.2×10^{-4} ng mL^{-1} to 3.2 ng mL^{-1} of CD44 with detection sensitivity of 1.4×10^{-2} pg mL^{-1}. The strong antifouling characteristics and robust practical workability further reflects the TiO_2/MX-$BiVO_4$ hybrids ideal candidacy for PEC biosensors.

Declaration of competing interest

The authors declare that they have no known competing financial interests or personal relationships that could have appeared to influence the work reported in this paper.

CRediT authorship contribution statement

Razium Ali Soomro: Conceptualization, Data curation, Formal analysis, Writing - original draft. **Sana Jawaid:** Methodology, Data

curation. **Nazar Hussain Kalwar:** Resources, Software, Investigation. **Mawada Tunesi:** Validation, Visualization, Data curation. **Selcan Karakuş:** Project administration, Writing - review & editing, Resources. **Ayben Kilislioğlu:** Project administration, Writing - review & editing, Software. **Magnus Willander:** Supervision, Validation.

Acknowledgments

This work was financially supported by the National Natural Science Foundation of China (NSFC, 51572011). The authors are thankful to Dr. Sidra Soomro from LUMS hospital Hyderabad, Pakistan in real-samples analysis.

Appendix A. Supplementary data

Supplementary data to this article can be found online at https://doi.org/10.1016/j.bios.2020.112439.

References

Antal, I., Koneracka, M., Kubovcikova, M., Zavisova, V., Khmara, I., Lucanska, D., Jelenska, L., Vidlickova, I., Zatovicova, M., Pastorekova, S., 2018. Colloids Surf., B 163, 236–245.
Carneiro, J., Döll-Boscardin, P.M., Fiorin, B.C., Nadal, J.M., Farago, P.V., Paula, J.P.d., 2016. Braz. J .Pharm. Sci. 52 (4), 645–651.
Chen, J., Huang, Q., Huang, H., Mao, L., Liu, M., Zhang, X., Wei, Y., 2020a. Nanoscale 12 (6), 3574–3592.
Chen, Y., Zhang, S., Dai, H., Hong, Z., Lin, Y., 2020b. Biosens. Bioelectron. 148, 111809.
Das, D., Makal, P., 2020. Appl. Surf. Sci. 506, 144880.
de Oliveira, S.A., da Silva, B.C., Riegel-Vidotti, I.C., Urbano, A., de Sousa Faria-Tischer, P.C., Tischer, C.A., 2017. Int. J. Biol. Macromol. 97, 642–653.
Derbali, M., Othmani, A., Kouass, S., Touati, F., Dhaouadi, H., 2020. Mater. Res. Bull. 125, 110771.
Fan, H., Zhou, H., Li, W., Gu, S., Zhou, G., 2020. Appl. Surf. Sci. 504, 144351.
Guo, Z., Li, P., Che, H., Wang, G., Wu, C., Zhang, X., Mu, J., 2016. Ceram. Int. 42 (3), 4517–4525.
Han, X., An, L., Hu, Y., Li, Y., Hou, C., Wang, H., Zhang, Q., 2020. Appl. Catal., B 265, 118539.
Huang, G., Li, S., Liu, L., Zhu, L., Wang, Q., 2020a. Appl. Surf. Sci. 503, 144183.
Huang, L., Zhou, X., Xue, R., Xu, P., Wang, S., Xu, C., Zeng, W., Xiong, Y., Sang, H., Liang, D., 2020b. Nano-Micro Lett. 12 (1), 44.
Ibrahim, I., Lim, H.N., Huang, N.M., Jiang, Z.-T., Altarawneh, M., 2020. J. Hazard Mater. 391, 122248.
Jiang, R., Chen, X., Deng, J., Wang, T., Wang, K., Chen, Y., Jiang, J., 2020. J. Energy Chem. 47, 79–85.
Koiki, B.A., Orimolade, B.O., Zwane, B.N., Nkosi, D., Mabuba, N., Arotiba, O.A., 2020. Electrochim. Acta 135944.
Kong, W., Guo, X., Jing, M., Qu, F., Lu, L., 2020. Biosens. Bioelectron. 150, 111875.
Li, Y., Chen, X., Sun, Y., Meng, X., Dall'Agnese, Y., Chen, G., Dall'Agnese, C., Ren, H., Sasaki, S., Tamiaki, H., 2020a. Adv. Mater. Interfaces 7, 1902080.
Li, Z., Jin, C., Wang, M., Kang, J., Wu, Z., Yang, D., Zhu, T., 2020b. Separ. Purif. Technol. 232, 115937.
Liang, Q., Ploychompoo, S., Chen, J., Zhou, T., Luo, H., 2020. Chem. Eng. J. 384, 123256.
Liu, P.P., Liu, X., Huo, X.H., Tang, Y., Xu, J., Ju, H., 2017. ACS Appl. Mater. Interfaces 9 (32), 27185–27192.
Lu, X., Sun, J., Sun, X., 2020. Trac. Trends Anal. Chem. 115882.
Lv, S., Zhang, K., Zhou, Q., Tang, D., 2020. Sensor. Actuator. B Chem. 310, 127874.
Polo, A., Grigioni, I., Dozzi, M.V., Selli, E., 2020. Catal. Today 340, 19–25.
Sang, X., Xie, Y., Lin, M.-W., Alhabeb, M., Van Aken, K.L., Gogotsi, Y., Kent, P.R.C., Xiao, K., Unocic, R.R., 2016. ACS Nano 10 (10), 9193–9200.
She, H., Yue, P., Ma, X., Huang, J., Wang, L., Wang, Q., 2020. Appl. Catal., B 263, 118280.
Shi, L., Xu, C., Jiang, D., Sun, X., Wang, X., Wang, Q., Zhang, Y., Qu, X., Du, F., 2018. Nanotechnology 30 (7), 075601.
Sinha, A., Dhanjai, Zhao, H., Huang, Y., Lu, X., Chen, J., Jain, R., 2018. Trac. Trends Anal. Chem. 105, 424–435.
Soleymaniha, M., Shahbazi, M.-A., Rafieerad, A.R., Maleki, A., Amiri, A., 2019. Adv. Healthc. Mater. 8 (1), 1801137.
Soomro, R.A., Jawaid, S., Zhu, Q., Abbas, Z., Xu, B., 2019. Chin. Chem. Lett. 31, 922–930.
Su, T., Hood, Z.D., Naguib, M., Bai, L., Luo, S., Rouleau, C.M., Ivanov, I.N., Ji, H., Qin, Z., Wu, Z., 2019. ACS Appl. Energy Mater. 2 (7), 4640–4651.
Sun, J., Li, X., Zhao, Q., Tadé, M.O., Liu, S., 2015. J. Mater. Chem. A 3 (43), 21655–21663.
Sun, Y., Meng, X., Dall'Agnese, Y., Dall'Agnese, C., Duan, S., Gao, Y., Chen, G., Wang, X.-F., 2019a. Nano-Micro Lett. 11 (1), 79.
Sun, Y., Sun, Y., Meng, X., Gao, Y., Dall'Agnese, Y., Chen, G., Dall'Agnese, C., Wang, X.-F., 2019b. Catal. Sci. Technol. 9 (2), 310–315.
Teranishi, M., Kunimoto, T., Naya, S.-i., Kobayashi, H., Tada, H., 2020. J. Phys. Chem. C 124 (6), 3715–3721.
Wang, R., Bai, J., Li, Y., Zeng, Q., Li, J., Zhou, B., 2017. Nano-Micro Lett. 9 (2), 14.
Wang, S., Li, S., Wang, W., Zhao, M., Liu, J., Feng, H., Chen, Y., Gu, Q., Du, Y., Hao, W., 2019. Sensor. Actuator. B Chem. 291, 34–41.
Xiao, R., Zhao, C., Zou, Z., Chen, Z., Tian, L., Xu, H., Tang, H., Liu, Q., Lin, Z., Yang, X., 2020. Appl. Catal., B 268, 118382.
Yan, D., Fu, X., Shang, Z., Liu, J., Luo, H.a., 2019. Chem. Eng. J. 361, 853–861.
Yu, L., Hu, L., Anasori, B., Liu, Y.-T., Zhu, Q., Zhang, P., Gogotsi, Y., Xu, B., 2018. ACS Energy Lett. 3 (7), 1597–1603.
Zalfani, M., van der Schueren, B., Hu, Z.-Y., Rooke, J.C., Bourguiga, R., Wu, M., Li, Y., Van Tendeloo, G., Su, B.-L., 2015. J. Mater. Chem. 3 (42), 21244–21256.
Zhang, H., Li, M., Zhu, C., Tang, Q., Kang, P., Cao, J., 2020a. Ceram. Int. 46 (1), 81–88.
Zhang, J., Wu, C., Li, T., Xie, C., Zeng, D., 2020b. Org. Electron. 77, 105504.
Zhang, P., Zhu, Q., Soomro, R.A., He, S., Sun, N., Qiao, N., Xu, B., 2020. Adv. Funct. Mater. 2000922.
Zhang, R., Rejeeth, C., Xu, W., Zhu, C., Liu, X., Wan, J., Jiang, M., Qian, K., 2019. Anal. Chem. 91 (11), 7078–7085.
Zhang, S., Shen, L., Ye, T., Kong, K., Ye, H., Ding, H., Hu, Y., Hua, J., 2020c. Energ, Fuel.
Zhou, Q., Tang, D., 2020. Trac. Trends Anal. Chem. 115814.
Zulkifili, A.N., Fujiki, A., Kimijima, S., 2018. Appl. Sci. 8 (2), 216.